ACS APPLIED MATERIALS & INTERFACES

Research Article

www.acsami.org

Self-Assembly of K_xWO_3 Nanowires into Nanosheets by an Oriented Attachment Mechanism

Shuangfeng Jia,[†] He Zheng,[†] Hongqian Sang,[†] Wenjing Zhang,[†] Han Zhang,[†] Lei Liao,[‡] and Jianbo Wang*[,†]

[†]School of Physics and Technology, Center for Electron Microscopy and MOE Key Laboratory of Artificial Micro- and Nano-structures, Wuhan University, Wuhan 430072, China

[‡]Department of Physics and Key Laboratory of Artificial Micro- and Nano-structures of Ministry of Education, Wuhan University, Wuhan 430072, China

Supporting Information

ABSTRACT: The K_xWO_3 nanosheets consisting of superfine nanowires were successfully synthesized in ambient air. The detailed electron microscopy and X-ray diffraction investigations imply that the nanosheets were obtained by self-assembly of the ordered nanowires with exposed $\{01\bar{1}0\}_H$ facets. The sheet morphology is closely related with the growth conditions including temperature and time, etc. A possible mechanism based on the oriented attachment of neighboring nanowires for the formation of nanosheets is proposed. Our results shed light on the interfacial characteristics of self-assembled K_xWO_3 nanowires and can serve as guidance to the future design of relevant two-dimensional structures for various electrical and optical applications.

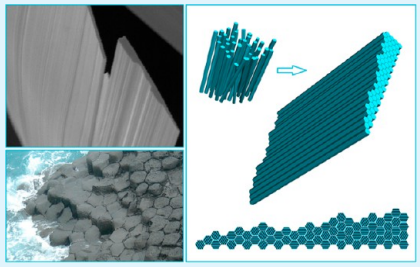

KEYWORDS: *K_xWO_3, oriented attachment, TEM, nanosheet*

1. INTRODUCTION

Two-dimensional (2D) nanosheets, which possess a nanoscale dimension only in thickness and have huge surface area, have been emerging as important new materials owing to their unique properties and various potential applications.[1−5] Studies in such exotic 2D systems recently intensified as a result of extensive investigations on graphene (carbon nanosheet), the molybdenum disulfide (MoS_2) nanosheet, and novel functionalities in metal oxide nanosheets.[4,6−9] Specifically, graphene has a high carrier mobility,[7] high values of Young's modulus,[10] and specific surface area.[11] Moreover, due to the 2D geometry, the ZnO nanosheet-based solar cell exhibits better performance than a nanoparticle-based solar cell or a well-oriented nanowire-based solar cell.[12] Another attractive aspect of the 2D nanosheets is that various nanostructures can be fabricated using them as building blocks.[13,14] Sophisticated functionalities or nanodevices can be designed through precise control of the arrangement of the selected nanosheets and combining materials at the molecular scale.

Nonetheless, compared to one-dimensional (1D) nanostructures, 2D nanostructures have not been explored in detail due to the difficulties associated with controllable nucleation and growth. Among several synthetic approaches for the preparation of the 2D nanostructures, two approaches have been widely employed: (1) the exfoliation method using scotch tape, that is, the micromechanical cleavage technique[8,9,15−17] and (2) the crystal growth method which controls the assembly of nanoparticle building blocks to form large nanosheets.[2,4,18−20] Semiconductor nanocrystals, such as CdTe,[18] PbS,[19] and WO_3,[20] can self-organize into free-standing nanosheets in a solution phase. The involved self-assembly of initially formed small nanocrystals was followed by a recrystallization process.[19,21] Comparing with nanoparticles, nanowires become more difficult to self-assemble into structures with orientational and/or positional order as a result of the extra possible configurations such as curling and twisting associated with these long and flexible nanostructures. To our best knowledge, nanosheets made by assembly of nanowires have been rarely reported because it is extremely difficult to integrate nonaligned nanowires onto nanowire-based devices. The well-ordered nanocomposites fabricated by molecular beam epitaxy (MBE) or other thin-film deposition technologies have limited commercial use because of their high costs and small scale grown area. Thus, the synthetic routes for the nanowires to self-assemble into nanosheets have attracted extensive attention. In parallel, it is also highly expected to explore the self-assembly mechanism from the nanowires to nanosheets.

Tungsten bronzes are known as multifunctional materials which can be potentially applied in electronic devices, optical devices, and rechargeable lithium batteries.[22−25] As is discussed above, the high surface-to-volume ratios of 2D nanostructures facilitate their potential for applications in electronic,[3] optical,[16] and different energy storage devices.[4,12,26,27] However, few

Received: August 14, 2013
Accepted: September 23, 2013
Published: September 23, 2013

studies on the tungsten bronze nanosheets have been reported because of the difficulty in synthesizing the nanosheets.

This work first provides a general route for the facile synthesis of single-crystalline hexagonal-based K_xWO_3 nanosheets based on oriented attachment of preformed pseudo-hexagonal K_xWO_3 nanowires. In subsequence, the self-assembly of superfine nanowires into nanosheets is revealed by X-ray diffraction (XRD), transmission electron microscopy (TEM), and micro Raman spectra investigations. A detailed discussion of the interfaces among nanowires is also presented, which further elucidates the attachment mechanism.

2. EXPERIMENTAL SECTION

The K_xWO_3 nanomaterials were synthesized by a simple method. First, a piece of cleaned W foil ($2 \times 2 \times 0.025$ cm^3) was sonicated in the KOH solution (0.05 mol dm^{-3}). The W foil was then heated on a hot plate under ambient conditions at 450 °C for 10 h and at 600 °C for 24 h, respectively, under which a vapor−solid mechanism governed the nanomaterial growth.

A FEI SIRION field emission scanning electron microscope (SEM) was used for morphological analysis for overall information and energy-dispersive spectroscopy (EDS) analysis. The XRD patterns were obtained by using the Bruker D8 Advance X-ray diffractometer with Cu Kα radiation (λ = 1.5418 Å). The micro Raman spectra were measured by a LabRAM HR800 Raman microspectrometer (λ_{laser} = 488 nm). The products were then scratched off the substrate and sonicated in ethanol, then dropped onto the holey carbon-coated copper grid for TEM observation. Bright-field (BF) imaging, dark-field imaging (DF), and selected area electron diffraction (SAED) were performed inside the JEOL JEM-2010 (HT) electron microscope. High-resolution transmission electron microscopy (HRTEM) images were taken by employing the JEOL JEM-2010FEF (UHR) electron microscope equipped with a field emission gun and Ω-type in-column energy filter system. Both microscopes were operated at the acceleration voltage of 200 kV.

3. RESULTS AND DISCUSSION

The morphology of the as-prepared K_xWO_3 was directly observed by using SEM. After being heated at 600 °C for 24 h in air, the pre-treated W foil was uniformly covered with numerous nanosheets which are up to tens of micrometers in width (Figure 1a). Figures 1b−d are SEM images of typical samples at different magnifications. The nanosheets mainly consist of K, W, and O as confirmed by EDS analysis (Figure S1, Supporting Information). Evidently, the nanosheets show the leaf-like structure with uneven surface (Figures 1b and 1c). The thickness of individual nanosheet ranges from 15 to 100 nm. As shown in Figure 1d, some thinner sheets can easily roll up. It is interesting to note that the nanosheet which has a rough surface can easily split into thin slices (pointed out by a black arrow in Figure 1c). What's more, the nanosheets consist of a bunch of nanowires with diameters spanning from 15 to 30 nm (indicated by the white arrow in Figure 1c). These nanowires partly fuse together and orient roughly parallel to each other. Thus, the nanosheets could be probably formed via the oriented attachment of numerous well-ordered and closely packed nanowires, which are similar to those previously reported in WO_3.[28,29]

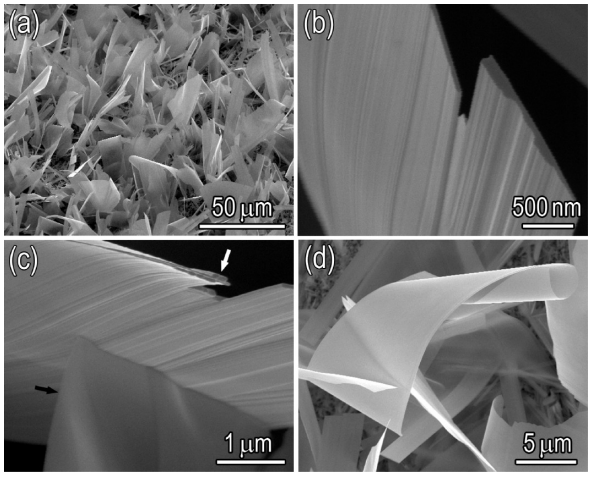

Figure 1. (a−d) SEM images of K_xWO_3 nanosheets taken at different magnifications.

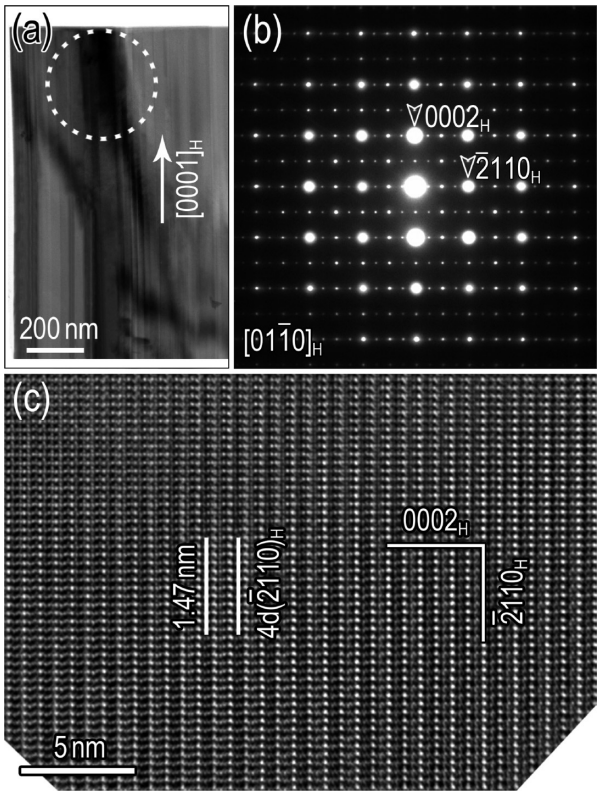

Figure 2. (a) BF TEM image of a K_xWO_3 nanosheet. (b) SAED pattern taken along the $[01\bar{1}0]_H$ zone axis, showing a pseudo hexagonal structure with the $[0001]_H$ growth direction. (c) An HRTEM image of the corresponding nanosheet.

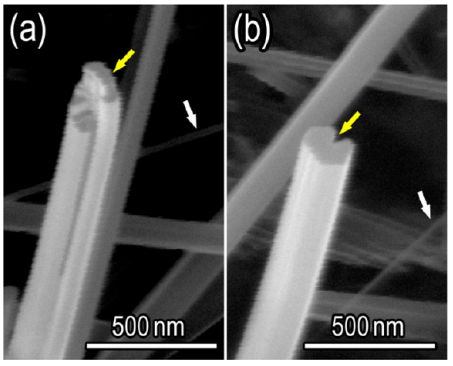

Figure 3. (a,b) SEM images of K_xWO_3 nanorods. The white arrows indicate superfine nanowires.

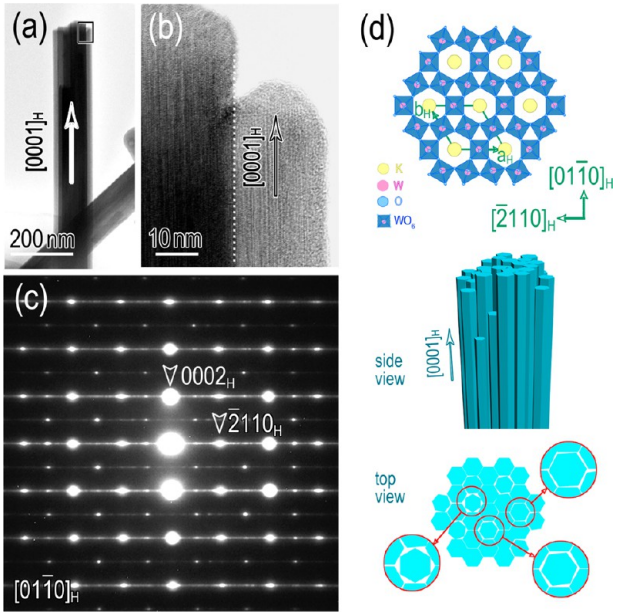

Figure 4. (a) BF TEM image of a K_xWO_3 nanorod. (b) Zoomed-in view of the framed area marked in (a). (c) SAED pattern taken along the $[01\bar{1}0]_H$ zone axis. (d) Structure of the K_xWO_3 framework projected along the *c* axis and schematic models for the nanorod.

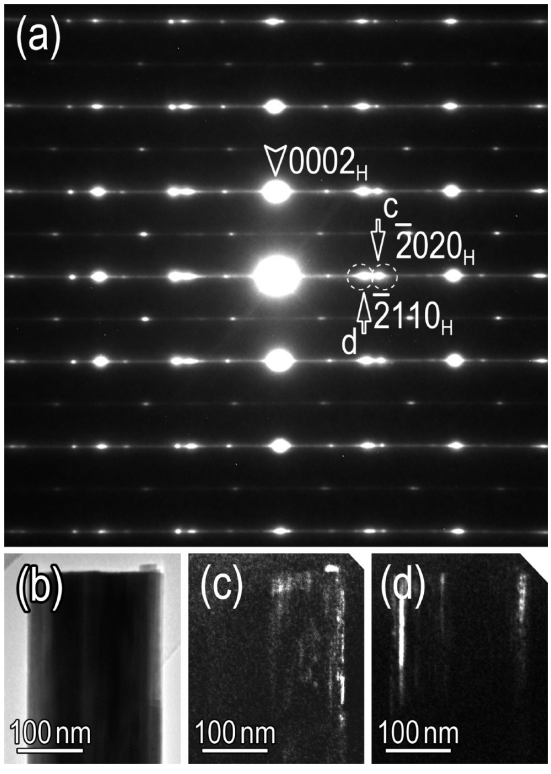

Figure 5. (a) SAED pattern of a nanorod. (b) Corresponding BF image of the nanorod. (c,d) DF images using $(\bar{2}020)_H$ and $(\bar{2}110)_H$ diffraction beams.

Figure 2a shows a typical BF image of the K_xWO_3 nanosheet. The corresponding SAED pattern taken from the area indicated by the dashed circle in Figure 2a is presented in Figure 2b. The major diffraction spots can be indexed as the $[01\bar{1}0]_H$ zone axis (the subscript "H" denotes the pseudo-hexagonal structure of K_xWO_3 with lattice parameters of a_H = 7.37 Å and c_H = 7.56 Å) (JCPDS 49-0541). The nanosheet grows along the $[0001]_H$ direction with exposed $\{01\bar{1}0\}_H$ surfaces. Besides the main diffraction spots, there exist four-fold satellite superstructure reflections (Figure 2b), implying the existence of an ordered superstructure. Further HRTEM inspection along the $[01\bar{1}0]_H$ zone axis (Figure 2c) verifies the existence of a four-fold superstructure in the K_xWO_3 nanosheet, as indicated by the interplanar spacing of 1.47 nm which is four times that of the $(\bar{2}110)_H$. Figure S2 (Supporting Information) shows the XRD pattern of the as-synthesized products. All diffraction peaks can be indexed well to a monoclinic super cell of K_xWO_3 with $\mathbf{a}_M = 4\mathbf{a}_H$, $\mathbf{b}_M = 2\mathbf{b}_H$, and $\mathbf{c}_M = \mathbf{c}_H$, where $\mathbf{a}_M$, $\mathbf{b}_M$, and $\mathbf{c}_M$ stand for the basic vectors of the monoclinic super cell of K_xWO_3 proposed by Goodman et al.[30] On the basis of their investigation, they proposed that the superstructure is caused by quadrupling of the a_H resulting from the ordering of the K vacancies and doubling of the b_H induced by small displacements of the tungsten atoms in WO_6 octahedra. A series of tilted SAED patterns and corresponding kinematic simulation of the composite patterns, as shown in Figure S3 (Supporting Information), demonstrate that three 120° twinning variants are presented in the ordered monoclinic phase. The coexistence of three monoclinic variants is verified by detailed TEM examination and will be discussed in detail in a separate paper.

To further understand the relevant growth mechanism, we have synthesized another batch of K_xWO_3 which was heated at lower temperature (450 °C) for less time (10 h) in air. The major products were nanorods with uniform one-dimensional morphologies. The nanorods are several micrometers long, and their diameters vary from 15 to 300 nm. Similar to the nanosheet, the nanorod consists of a bunch of superfine nanowires (indicated by a yellow arrow in Figure 3a), the diameters of which range from 15 to 30 nm as indicated by white arrows in Figures 3a and 3b. Meanwhile, the cross section of some nanorod is a polygon with a triangular gap which is pointed out by a yellow arrow in Figure 3b. Figure 4a shows a typical BF image of an individual nanorod. The end of the nanorod demonstrates uneven characteristics which can provide further insight into the morphological and microstructural details of the nanorods. The enlarged TEM image reveals that the nanorod consists of neighboring nanowires which are attached to each other with different lengths (as indicated by the dotted line in Figure 4b). This phenomenon can be attributed to the different growth rates of the wires. Figure 4c shows the typical SAED pattern of the K_xWO_3 nanorod, which is indexed based upon the basic hexagonal K_xWO_3 structure. The growth direction of the hexagonal K_xWO_3 nanorod can be identified as $[0001]_H$ based on the BF TEM image and corresponding SAED pattern. Numerous satellite diffraction spots and the elongated lines perpendicular to the growing direction are observed in addition to the basic hexagonal diffraction spots. Intensity profiles of two typical SAED patterns which are presented in Figure S4 (Supporting Information) indicate that these satellite diffraction spots involve four-fold superstructure diffraction spots outlined by a dashed line and other l_H = 0 diffraction spots marked by red arrows. On the basis of the results discussed above, a schematic model for the growth of the K_xWO_3 nanorod is depicted in Figure 4d. The nanorod consists of superfine nanowires attached to each other with different lengths. In the crystalline-equivalent hexagonal K_xWO_3 system, considering the typical hexagonal tunnel structure, the as-synthesized nanowires have an ideal hexagonal-shaped cross section with

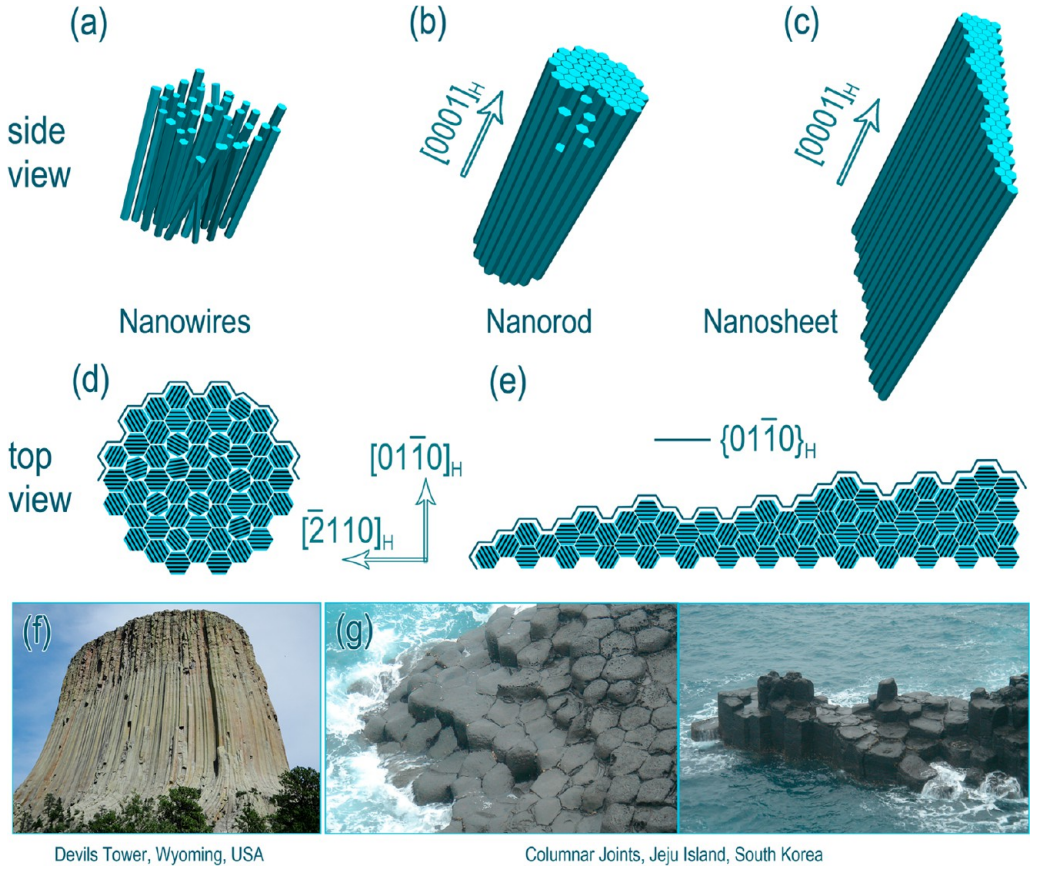

Figure 6. Schematic illustration of the growth mechanism of K_xWO_3 nanostructures. Three main stages of nanostructure growth are shown: (a) nanowire growth, (b) nanorod growth, and (c) nanosheet growth. (d) and (e) are top views of the K_xWO_3 nanorod and nanosheet, respectively. The morphology of K_xWO_3 nanomaterials is similar to columnar basalt formations like (f) Devils Tower and (g) the Columnar Joints.

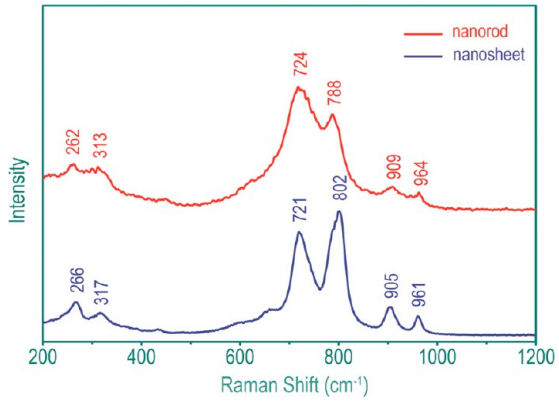

Figure 7. Micro Raman spectra of a K_xWO_3 nanorod (red line) and a K_xWO_3 nanosheet (blue line).

six $\{01\bar{1}0\}_H$ facets which is confirmed by the BF image of a nanosheet cross-section and corresponding SAED pattern (Figure S5, Supporting Information). Under the lower growth temperature, rotation misalignment angles between $\{01\bar{1}0\}_H$ facets might be present (Figure 4d). Thus, satellite diffraction spots and elongated lines in the SAED patterns should result from the defects and/or disordering formed during the course of nanowire assembly. Figure 5a shows another typical SAED pattern of an individual nanorod. Compared with the corresponding BF image (Figure 5b), the DF images by using $(\bar{2}110)_H$ (Figure 5c) and $(\bar{2}020)_H$ (Figure 5d) diffraction beams clearly demonstrate that the nanorod consists of several nanowires.

On the basis of these observations, it can be concluded that K_xWO_3 nanosheets actually evolved from the oriented attachment of the K_xWO_3 nanowires. It is noted that the oriented attachment mechanism has been applied to explain the growth of various oriented and hierarchical nanostructures via self-assembly of nanocrystals.[21,31] According to the mechanism, primary particles may aggregate in an oriented fashion to produce a larger single crystal, or they may aggregate randomly and reorient, recrystallize, or undergo phase transformations to produce larger single crystals. In the nucleated aggregates, the crystalline lattice planes may be almost perfectly aligned, or dislocations at the contact areas between the adjacent nanowires lead to defects in the final crystals. In the current case, as the growth temperature rises, the K_xWO_3 nanosheets consist of a bunch of parallel-aligned nanowires with $[0001]_H$ growth direction and exhibit better crystallinity. The parallel-aligned nanowires in nanosheets are equivalent to different twinning variants which possess smooth prismatic side $\{01\bar{1}0\}_H$ facets with low surface energy.

Figure 6 schematically shows the possible mechanism that corresponds to the transformation of K_xWO_3 nanostructures from wires to sheet. At the initial stage of this process, K_xWO_3 nanowires enclosed by six $\{01\bar{1}0\}_H$ facets began to nucleate and grow along the $[0001]_H$ direction (Figure 6a). As the reaction time increases, the neighboring K_xWO_3 nanowires tend to coalesce together to minimize the surface energy, which forms self-assembled K_xWO_3 nanosheets. On the basis of a previous

discussion, at a lower growth temperature and less reaction time, the density of K_xWO_3 species is lower, and the growth rate of nanowires is slow. The surface energy of the nanowires is only adequate for the nanowires to align side-by-side and to form nanowire bundles. Thus, nanorods are formed by self-assembly of nanowires with twist and rotation misalignment around their $[0001]_H$-oriented direction (Figures 6b and 6d). With high growth temperature and more reaction time, nucleation could occur in any appropriate direction accompanied with the increased density of K_xWO_3 species. The different close-packing rates between the $\{01\bar{1}0\}_H$ and $\{\bar{2}110\}_H$ planes in the basic hexagonal K_xWO_3 lead to the notably different growth rates in the two directions of the cross sections (i.e., $[01\bar{1}0]_H$ and $[\bar{2}110]_H$), and thus the nanosheets with a large width-to-thickness ratio were formed (Figures 6c and 6e). Recrystallization of an interface layer to accommodate the lattice mismatch between neighboring nanowires and the rolling of neighboring nanowires to eliminate interface energy to form a single-crystal nanosheet might occur simultaneously (Figures 6c and 6e). It is reasonable that the surfaces of both nanorods and nanosheets are uneven since the nanowires with exposed $\{01\bar{1}0\}_H$ surfaces generally have hexagonal prism morphology with the top view shown in Figures 6d and 6e. The ordering of K vacancies along the $<\bar{2}110>_H$ direction in each variant is indicated by black stripes on the schematic diagrams (Figures 6d and 6e). Figure 6d shows the arrangement of the nanowires in the nanorod which exhibits a little disordering with different rotation angles around the $[0001]_H$ axis. In contrast, the arrangement of nanowires in the nanosheet is more ordering as shown in Figure 6e. All exposed surfaces of nanostructures and the interface of neighboring nanowires are enclosed by $\{01\bar{1}0\}_H$ planes, resulting in the zigzag-shaped interfaces (Figure 6e), which cannot be edge-on viewed in the TEM. It is interesting to note that the morphology of K_xWO_3 nanomaterials is similar to spectacular natural geological wonders with columnar basalt formations like Devils Tower and the Columnar Joints, etc. (Figures 6f and 6g).

The micro Raman spectra shown in Figure 7 are taken from the nanorod (red line) and nanosheet (blue line) samples with a conventional photon counting system. There are three groups of Raman peaks in the regions of 900−970, 700−820, and 200−400 cm^{-1}, which could be assigned to W═O stretching, O−W−O stretching, and O−W−O bending modes, respectively. The appearance of the two Raman bands in the 900−970 cm^{-1} region indicates the presence of terminal W═O bonds, which support the conclusions that the structure of pseudo-hexagonal K_xWO_3 nanomaterials contains W vacancies.[32,33] Obviously, the broadening of the observed Raman peaks for nanosheets which are significantly narrower than those observed previously for nanorods is caused by both the disorder and defects produced in the aggregation process of the nanowires. Therefore, the Raman spectra suggest that the self-assembled K_xWO_3 nanosheets are highly crystalline.

4. CONCLUSION

In summary, high crystalline K_xWO_3 nanosheets with pseudo-hexagonal structure have been synthesized via a simple heating method. The detailed structural characterization of the interfaces among K_xWO_3 nanowires indicates that the nanosheets are formed via the self-assembly of individual nanowires by $\{01\bar{1}0\}_H$ facets. In the case that the growth temperature is high enough, the arrangement of the nanowires becomes more ordered, leading to a single-crystal nanosheet. The interfacial characteristics of K_xWO_3 nanowires may offer a fundamental insight into the related electrical and optical properties of two-dimensional nanosheets or nanofilms.[34]

■ ASSOCIATED CONTENT

Supporting Information

Detailed microstructural characterization of K_xWO_3 nanostructures, EDS spectrum, and XRD patterns of the K_xWO_3 nanosheet. This material is available free of charge via the Internet at http://pubs.acs.org.

■ AUTHOR INFORMATION

Corresponding Author

*E-mail: wang@whu.edu.cn.

Notes

The authors declare no competing financial interest.

■ ACKNOWLEDGMENTS

This work was supported by the 973 Program (2011CB933300), National Natural Science Foundation of China (51271134, 51071110, 40972044, J1210061), China MOE NCET Program (NCET-07-0640), MOE Doctoral Fund (20090141110059), and the Fundamental Research Funds for the Central Universities.

■ REFERENCES

(1) Guo, S. J.; Dong, S. J.; Wang, E. K. *ACS Nano* **2010**, *4*, 547−555.
(2) Yan, H.; Yu, Z.; Lu, K.; Zhang, Y. J.; Wei, Z. X. *Small* **2011**, *7*, 3472−3478.
(3) Ye, Y.; Yu, B.; Gao, Z. W.; Meng, H.; Zhang, H.; Dai, L.; Qin, G. G. *Nanotechnology* **2012**, *23*, 194004.
(4) Wang, C.; Zhou, Y.; Ge, M. Y.; Xu, X. B.; Zhang, Z. L.; Jiang, J. Z. *J. Am. Chem. Soc.* **2010**, *132*, 46−47.
(5) Hu, Z.; Ji, Z.; Lim, W.; Mukherjee, B.; Zhou, C.; Tok, E. S.; Sow, C. H. *ACS Appl. Mater. Interfaces* **2013**, *5*, 4731−4738.
(6) Geim, A. K. *Science* **2009**, *324*, 1530−1534.
(7) Novoselov, K. S.; Geim, A. K.; Morozov, S. V.; Jiang, D.; Zhang, Y.; Dubonos, S. V.; Grigorieva, I. V.; Firsov, A. A. *Science* **2004**, *306*, 666−669.
(8) Coleman, J. N.; Lotya, M.; O'Neill, A.; Bergin, S. D.; King, P. J.; Khan, U.; Young, K.; Gaucher, A.; De, S.; Smith, R. J.; et al. *Science* **2011**, *331*, 568−571.
(9) Bertolazzi, S.; Brivio, J.; Kis, A. *ACS Nano* **2011**, *5*, 9703−9709.
(10) Lee, C.; Wei, X. D.; Kysar, J. W.; Hone, J. *Science* **2008**, *321*, 385−388.
(11) Stoller, M. D.; Park, S. J.; Zhu, Y. W.; An, J. H.; Ruoff, R. S. *Nano Lett.* **2008**, *8*, 3498−3502.
(12) Xiang, J. H.; Zhu, P. X.; Masuda, Y.; Okuya, M.; Kaneko, S.; Koumoto, K. *J. Nanosci. Nanotechnol.* **2006**, *6*, 1797−1801.
(13) Tanaka, T.; Fukuda, K.; Ebina, Y.; Takada, K.; Sasaki, T. *Adv. Mater.* **2004**, *16*, 872−875.
(14) Qiu, J. H.; Guo, M.; Wang, X. D. *ACS Appl. Mater. Interfaces* **2011**, *3*, 2358−2367.
(15) Osada, M.; Sasaki, T. *J. Mater. Chem.* **2009**, *19*, 2503−2511.
(16) Fukuda, K.; Akatsuka, K.; Ebina, Y.; Osada, M.; Sugimoto, W.; Kimura, M.; Sasaki, T. *Inorg. Chem.* **2012**, *51*, 1540−1543.
(17) Nicolosi, V.; Chhowalla, M.; Kanatzidis, M. G.; Strano, M. S.; Coleman, J. N. *Science* **2013**, *340*, 1226419.
(18) Tang, Z. Y.; Zhang, Z. L.; Wang, Y.; Glotzer, S. C.; Kotov, N. A. *Science* **2006**, *314*, 274−278.
(19) Schliehe, C.; Juarez, B. H.; Pelletier, M.; Jander, S.; Greshnykh, D.; Nagel, M.; Meyer, A.; Foerster, S.; Kornowski, A.; Klinke, C.; et al. *Science* **2010**, *329*, 550−553.
(20) Chen, X. Y.; Zhou, Y.; Liu, Q.; Li, Z. D.; Liu, J. G.; Zou, Z. G. *ACS Appl. Mater. Interfaces* **2012**, *4*, 3372−3377.

(21) Liao, H. G.; Cui, L. K.; Whitelam, S.; Zheng, H. M. *Science* **2012**, *336*, 1011−1014.
(22) Zheng, Z.; Yan, B.; Zhang, J.; You, Y.; Lim, C. T.; Shen, Z.; Yu, T. *Adv. Mater.* **2008**, *20*, 352−356.
(23) Wechter, M. A.; Shanks, H. R.; Carter, G.; Ebert, G. M.; Guglielmino, R.; Voigt, A. F. *Anal. Chem.* **1972**, *44*, 850−853.
(24) Martinez-de La Cruz, A.; Torres, L. G. C. *Ceram. Int.* **2008**, *34*, 1779−1782.
(25) Tsuyumoto, I.; Kudo, T. *Mater. Res. Bull.* **1996**, *31*, 17−28.
(26) Mariotti, D.; Lindstrom, H.; Bose, A. C.; Ostrikov, K. *Nanotechnology* **2008**, *19*, 495302.
(27) Su, Y. Z.; Li, S.; Wu, D. Q.; Zhang, F.; Liang, H. W.; Gao, P. F.; Cheng, C.; Feng, X. L. *ACS Nano* **2012**, *6*, 8349−8356.
(28) Su, C. Y.; Lin, H. C. *J. Phys. Chem. C* **2009**, *113*, 4042−4046.
(29) Ko, R. M.; Wang, S. J.; Tsai, W. C.; Liou, B. W.; Lin, Y. R. *CrystEngComm* **2009**, *11*, 1529−1531.
(30) Goodman, P. *Acta Crystallogr., Sect. B* **1976**, *32*, 3280−3285.
(31) Cho, K. S.; Talapin, D. V.; Gaschler, W.; Murray, C. B. *J. Am. Chem. Soc.* **2005**, *127*, 7140−7147.
(32) Maczka, M.; Hanuza, J.; Waskowska, A. *J. Raman Spectrosc.* **2003**, *34*, 432−437.
(33) Coelho, J. S.; Paraguassu, W.; Maczka, M.; Souza, A. G.; Freire, P. T. C.; Mendes, J.; Hanuza, J. *J. Raman Spectrosc.* **2009**, *40*, 1150−1157.
(34) Jiang, Q. K.; Zheng, H.; Wang, J. B.; Long, H.; Fang, G. J. *ACS Appl. Mater. Interfaces* **2012**, *4*, 7042−7045.